Supporting Information

Single Organic Droplet Collision Voltammogram

via Electron Transfer Coupled Ion Transfer

Cheng Liu,[1,†] Pekka Peljo,[2,†] Xinjian Huang,[1] Wenxue Cheng,[1] Lishi Wang,*[1] Haiqiang Deng,*[3]

[1]School of Chemistry and Chemical Engineering, South China University of Technology, Guangzhou 510641, China

[2]Laboratoire d'Electrochimie Physique et Analytique, École Polytechnique Fédérale de Lausanne (EPFL Valais Wallis), Rue de I'Industrie, 17, 1951 Sion, Switzerland

[3]Institute of Chemistry, The Hebrew University of Jerusalem, Jerusalem 9190401, Israel

[†]Equal contribution.

*Corresponding authors: E-mail: wanglsh@scut.edu.cn (L.S. Wang); E-mail: haiqiang.deng@mail.huji.ac.il or hqdeng2010@gmail.com (H.Q. Deng).

Table of Contents

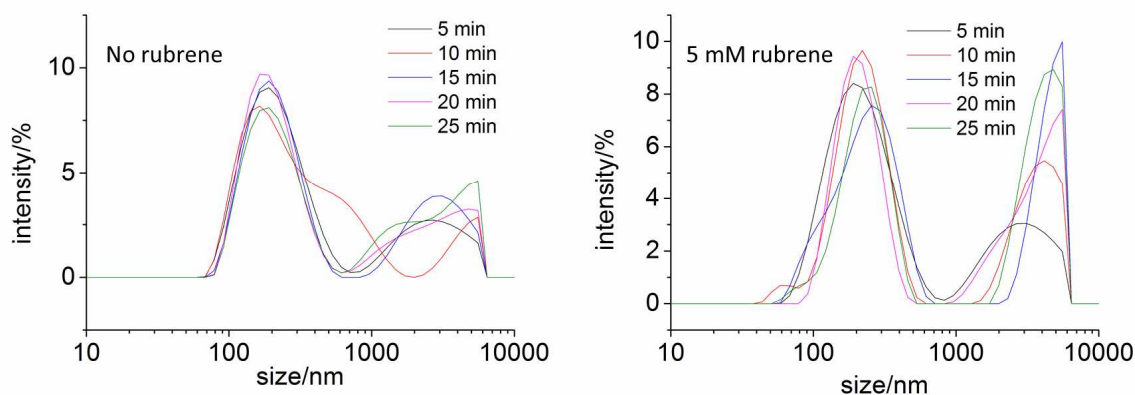# 1. Emulsion Size Distributions Determined by DLS

Figure S1. The size distributions (in diameter) of toluene (with and without 5 mM rubrene in 400 mM IL–PA)/water emulsion droplets determined by dynamic light scattering (DLS). The emulsion samples (detailed in the Experimental Section in the main text) were diluted by the factor of 4 to obtain better sensitivity.

2. Thermodynamic Calculations for Ionic Phase Distribution

The initial distribution of salts between aqueous and toluene phases can be calculated as described by Kakiuchi.[1] The Nernst equation describes the distribution of ions at liquid–liquid interfaces:

$$\Delta_o^w \phi = \Delta_o^w \phi_i^{0'} + \frac{RT}{z_i F} \ln \frac{c_i^o}{c_i^w} \tag{1}$$

where $\Delta_o^w \phi$ is the Galvani potential difference between the aqueous and organic phases, $\Delta_o^w \phi_i^{0'}$ is the formal ion transfer potential of species i, R, T and F are the molar gas constant, thermodynamic temperature and Faraday constant, c_i and z_i are the concentration and charge

(with the sign) of the species i, and superscripts "o" and "w" refer to oil (*viz.* toluene) and aqueous phases. The mass balance equation for species i is

$$n_{i,\text{tot}} = n_i^{\text{o}} + n_i^{\text{w}} \tag{2}$$

and hence

$$V^{\text{o}}c_{i,\text{init}}^{\text{o}} + V^{\text{w}}c_{i,\text{init}}^{\text{w}} = V^{\text{o}}c_i^{\text{o}} + V^{\text{w}}c_i^{\text{w}} \tag{3}$$

where n is the molar amount and V is volume, and subscripts "tot" and "init" refer to total and initial status. Additionally, the electroneutrality of both phases is assumed to hold:

$$\sum_i z_i c_i^{\text{w}} = \sum_i z_i c_i^{\text{o}} = 0 \tag{4}$$

Combination of Eq. 1 to 4 gives:

$$\sum_i z_i \frac{V^{\text{o}}c_{i,\text{init}}^{\text{o}} + V^{\text{w}}c_{i,\text{init}}^{\text{w}}}{V^{\text{w}} + V^{\text{o}} \exp\left[\frac{z_i F}{RT}\left(\Delta_{\text{o}}^{\text{w}}\phi - \Delta_{\text{o}}^{\text{w}}\phi_i^{0'}\right)\right]} = 0 \tag{5}$$

This equation contains only one unknown variable, $\Delta_{\text{o}}^{\text{w}}\phi$, that can be evaluated numerically.

Concentration of species can be solved from Eq. 1 and 3 when $\Delta_{\text{o}}^{\text{w}}\phi$ is known.

The formal ion transfer potentials for the ions studied in this paper are not known, but fortunately they can be estimated from the linear relationship of the Gibbs energies of transfer between water and two different immiscible nonaqueous solvents. The formal ion transfer potentials of ions for water–toluene interface were converted to apparent Gibbs energy of transfer $\Delta G_{i,\text{app}}^{\text{w}\to\text{o}} = z_i F \Delta_{\text{o}}^{\text{w}}\phi_i^{0'}$ (not taking into account the effects of activities or ion pairing), and the plot of the $\Delta G_{i,\text{app}}^{\text{w}\to\text{toluene}}$ *vs.* $\Delta G_i^{\text{w}\to\text{DCE}}$ is shown in Figure S2.[2] Note that DCE is abbreviated to 1,2-dichloroethane. The corresponding values are tabulated in Table S1.
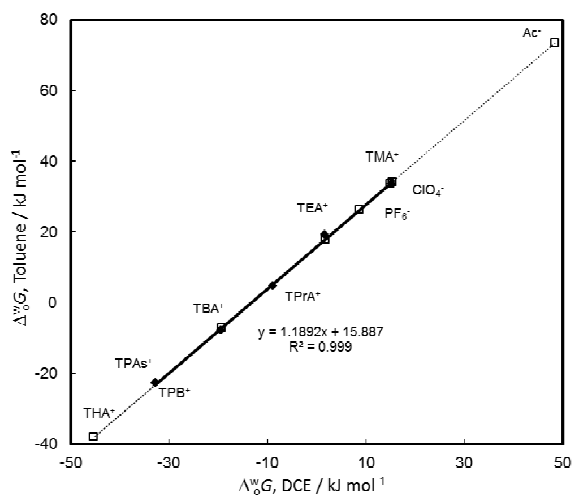
Figure S2. Linear correlation of the apparent Gibbs energy of transfer of ions from aqueous phase into toluene and the standard Gibbs energy of transfer of ions from aqueous phase into DCE. Solid points: experimental data. Open squares: Extrapolation.

Table S1. Transfer energies from water to DCE, apparent transfer energies from water to toluene and the formal ion transfer potentials between water and toluene. The anion of the ionic liquid IL-PA composed of trihexyltetradecylphosphonium (P_{66614}^{+}) and bis(trifluoromethylsulfonyl)amide (NTf_2^{-}) is also included.

Ion	$\Delta G_i^{\text{w}\rightarrow\text{DCE}}$, kJ mol^{-1}	$\Delta G_i^{\text{w}\rightarrow\text{toluene}}$ kJ mol^{-1}	$\Delta_{\text{toluene}}^{\text{w}}\phi_i^{0'}$, V
TMA$^+$	15.4[a]	34.2	0.354
TEA$^+$	1.8[a]	18.0	0.187
TBA$^+$	−19.3[a]	−7.06	−0.073
THA$^+$	−45.3[a]	−38.0	−0.393
PF$_6^-$	8.7[b]	26.2	−0.271
ClO$_4^-$	14.9[a]	33.6	−0.348
Ac$^-$	48.4[a]	73.4	−0.761
NTf$_2^-$	−3.1[c]	12.2	−0.127

[a]Values from the database of the Prof. Girault's group, http://sbsrv7.epfl.ch/instituts/isic/lepa/cgi/DB/InterrDB.pl
[b]Ref.[3]

[c] Ref.[4] recalculated with $\Delta G_{\text{ClO}_4^-}^{\text{w}\rightarrow\text{DCE}}$ = 14.9 kJ mol^{-1}

As the transfer of P_{66614}^+ is not observed experimentally at the potential up to 1.3 V, its ion transfer potential has to be significantly less than that of Ac^-. Hence, the transfer of this cation was not considered in this study.

The composition of the aqueous and toluene phases can be calculated with the data from Table S1, in combination with equations (1) to (5). Note that volume of the organic phase is 0.1 mL and the volume of the aqueous phase is 5 mL for preparing the emulsion for electrochemical collision measurements. The results are tabulated in Table S2.

Table S2. Equilibrium concentrations and the Galvani potential differences for different electrochemical collision experiments from Figures 1 and 2 in the main text and Figure S16, $T =$ 298.15 K.

Salt	c_{init}^w, mM	c_{init}^o, mM	$\Delta_{toluene}^w \phi$, V	c_{eq}^w, mM	c_{eq}^o, mM
TEAPF$_6$	0	5	−0.043	0.1	1.3×10^{-5}
TBAPF$_6$	0	5	−0.173	0.1	0.002
THAPF$_6$	0	5	−0.333	0.082	0.881
TBAClO$_4$	5	0	−0.211	5	0.024
TBAAc	5	0	−0.417	5	7.7×10^{-6}
TMAPF$_6$	5	0	0.041	5	2.5×10^{-5}
TBAAc	0.1	0	−0.417	0.1	1.5×10^{-7}
TBAAc	0.5	0	−0.417	0.5	7.7×10^{-7}
TBAAc	50	0	−0.417	50	7.7×10^{-5}
TBAAc	100	0	−0.417	100	1.5×10^{-4}
TBAAc	200	0	−0.417	200	3.1×10^{-4}

3. Peak Current Distributions and Analysis

Figure S3 shows the oxidation peak current distribution for all the electrochemical collision measurements in the presence of a myriad of salts in either aqueous or toluene droplets. The Gaussian distribution with the parameters included in the figure is given as a guide for the eye, as the data is a bit scattered for accurate fitting. The corresponding DLS data is given in Figure S4.
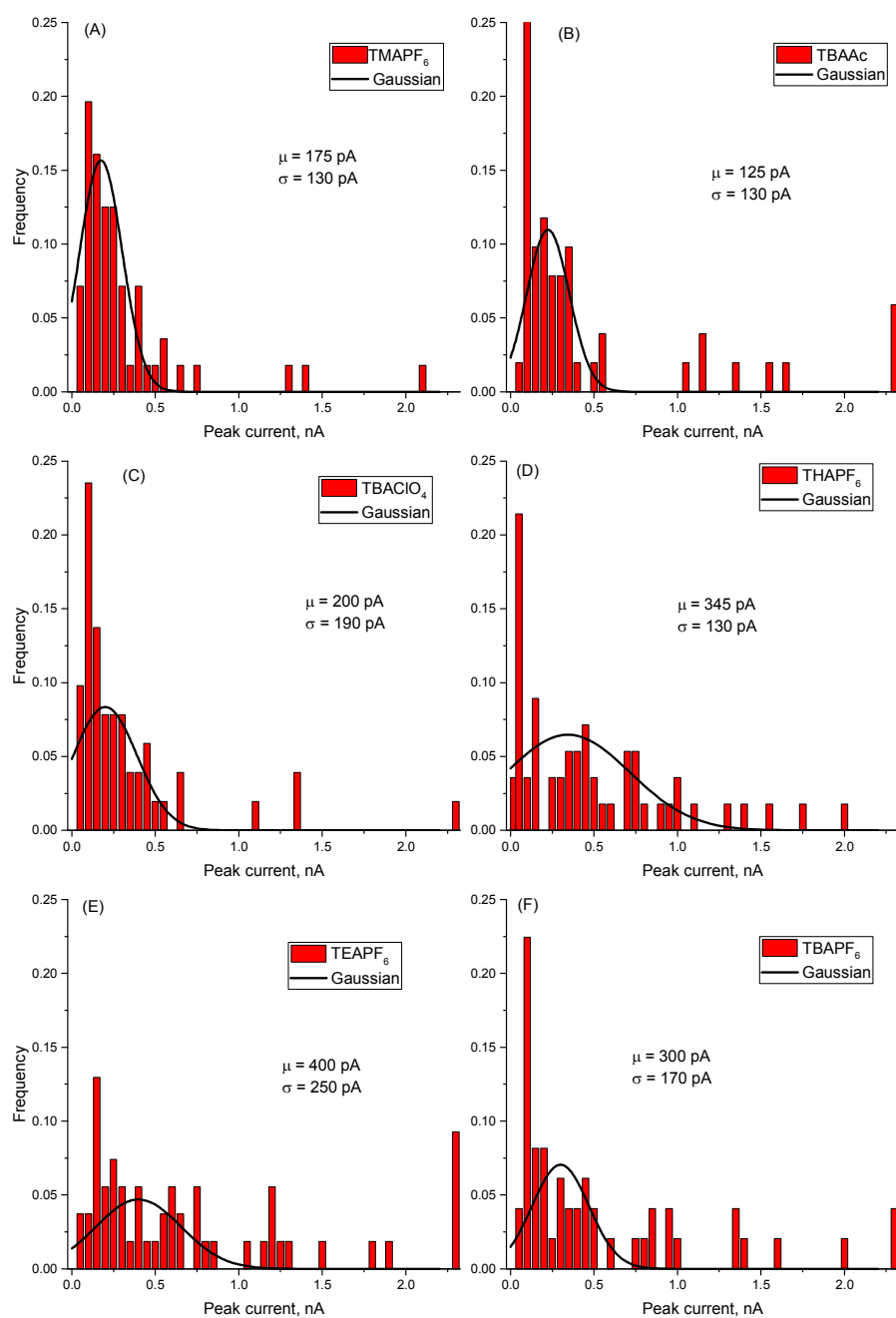
Figure S3. The peak current distribution for the oxidation peaks obtained with FSCV at 40 V/s for the different salts (A) $TMAPF_6$ (B) TBAAc (C) $TBAClO_4$ (D) $THAPF_6$ (E) $TEAPF_6$ (F) $TBAPF_6$. The Gaussian distribution with the parameters included in the figure is given as a guide for the eye.
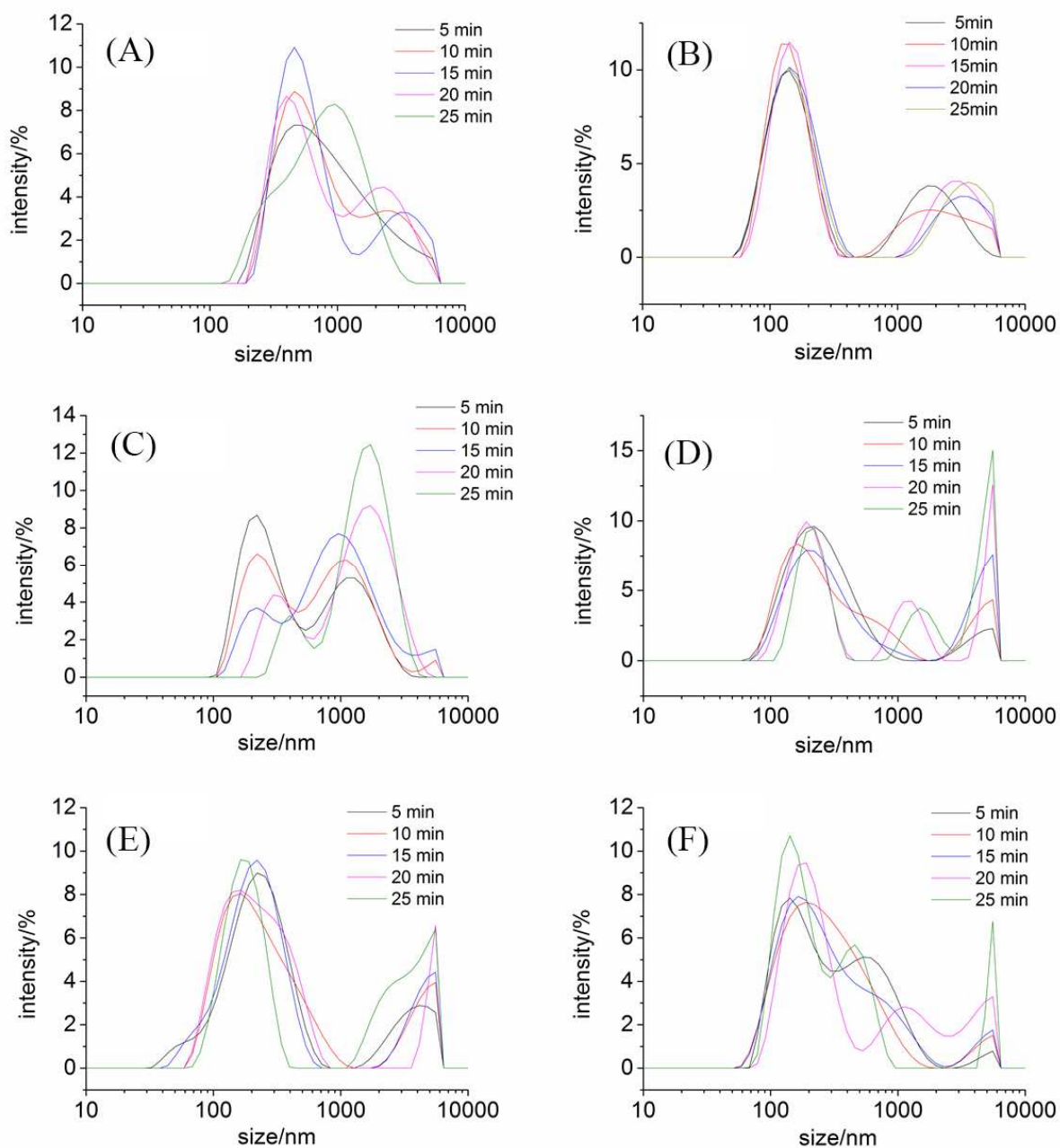
Figure S4. The DLS data monitored as a function of time for emulsions made with 25 μL of organic phase in 5 mL of the aqueous phase: (A) TMAPF$_6$ (B) TBAAc (C) TBAClO$_4$ (D) THAPF$_6$ (E) TEAPF$_6$ (F) TBAPF$_6$.

Finite element simulations show that FSCV of a droplet below 1 μm in diameter has a peak current of less than 100 pA, so small droplets are difficult to detect with the FSCV. Figure S5

gives a specific example (for Figure S3) of a group of recovered FSCVs with varied peak currents obtained by the electrochemical emulsion droplets collisions in the presence of 5 mM TBAAc in aqueous. Table S3 is the summary of peak currents of recovered FSCVs from Figure 1 in the main text obtained with different kinds of ions.
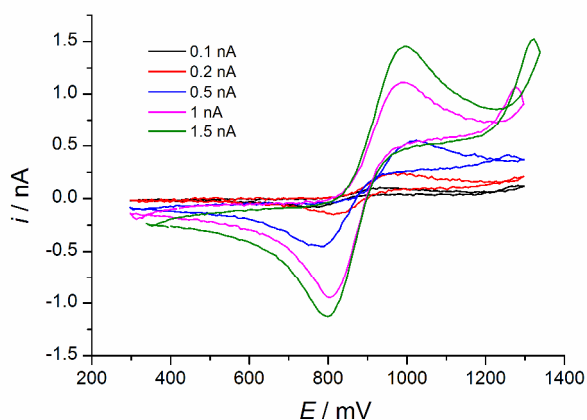

Figure S5. An example of the FSCVs obtained for five emulsion droplets colliding on the C UME with varied peak currents in which 5 mM TBAAc is initially added in the aqueous phase.

Table S3. Peak currents summary of recovered cyclic voltammograms from Figure 1 in the main text *via* single emulsion droplet collision experiments with addition of different kinds of ions.

I_{pa}	I_{pc}	I_{pa}/I_{pc}	I_{pa}	I_{pc}	I_{pa}/I_{pc}	I_{pa}	I_{pc}	I_{pa}/I_{pc}
1.293	1.112	1.16	3.333	3.71	0.90	0.152	0.121	1.26
1.379	1.193	1.16	1.52	1.529	0.99	0.174	0.12	1.45
0.063	0.05	1.26	0.262	0.3	0.87	0.3	0.27	1.11
0.227	0.167	1.36	2.394	2.72	0.88	0.425	0.382	1.11
0.16	0.115	1.39	1.638	1.902	0.86	2.827	2.646	1.07
0.385	0.325	1.18	0.22	0.258	0.85	0.145	0.138	1.05

(column groups: TMAPF$_6$ | TBAAc | TBAClO$_4$)

I_{pa}	I_{pc}	I_{pa}/I_{pc}		I_{pa}	I_{pc}	I_{pa}/I_{pc}		I_{pa}	I_{pc}	I_{pa}/I_{pc}
0.225	0.15	1.50		0.105	0.11	0.95		0.12	0.11	1.09
0.264	0.226	1.17		0.376	0.408	0.92		0.131	0.119	1.10
0.136	0.112	1.21		0.333	0.401	0.83		0.632	0.649	0.97
0.367	0.292	1.26		1.115	1.339	0.83		0.152	0.121	1.26
0.158	0.114	1.39		2.679	3.272	0.82				
				0.169	0.204	0.83				

THAPF$_6$				TBAPF$_6$				TEAPF$_6$		
I_{pa}	I_{pc}	I_{pa}/I_{pc}		I_{pa}	I_{pa}	I_{pa}/I_{pc}		I_{pa}	I_{pc}	I_{pa}/I_{pc}
0.441	0.437	1.01		0.323	0.368	0.88		1.766	2.06	0.86
0.703	0.681	1.03		1.994	2.082	0.96		0.103	0.12	0.86
1.287	1.277	1.01		0.268	0.262	1.02		0.099	0.101	0.98
0.237	0.193	1.23		0.413	0.392	1.05		0.5	0.537	0.93
0.941	0.794	1.19		0.182	0.164	1.11		0.439	0.471	0.93
0.45	0.364	1.24		0.258	0.246	1.05		0.141	0.125	1.13
0.309	0.252	1.27		5.274	5.45	0.97		1.17	1.3	0.90
0.653	0.558	1.17		0.922	0.911	1.01		0.281	0.295	0.95
				1.362	1.309	1.04		0.129	0.107	1.21
				0.464	0.458	1.01		1.183	1.232	0.96
				0.843	0.852	0.99		1.199	1.421	0.84

4. Collision Frequency Analysis

The experimental collision frequency in Figure 1 in the main text is summarized in Table S4. The theoretical collision frequency of the emulsion droplets or oil particles dictated by mass transfer solely from diffusion to an infinite UME surface – $f_{p,s}$ can be estimated by Eq. 6 and 7,[5] being 0.11 Hz tabulated in Table S4.

$$f_{p,s} = 4D_p c_p r_{UME} N_A \tag{6}$$

$$D_p = \frac{k_B T}{6\pi\eta r_p} \tag{7}$$

where D_p is the diffusion coefficient of the oil particles/droplets, c_p is the molar concentration of the oil droplets, r_{UME} is the radius of the carbon UME, N_A is Avogadro's number, k_B is the Boltzmann constant, T has been defined, η is the dynamic viscosity of water at 298.15 K (0.89 × 10^{-3} kg·m^{-1}s^{-1}),[6] and r_p is the modal/nominal radius (taking 1 μm for an example) of the oil droplets in the bulk aqueous determined by DLS (Figure S4). It is seen from Table S4 that only in the TMAPF$_6$ case the experimental collision frequency is higher than (but if we consider the fluctuations in this stochastic process, it is in line with) the theoretical one, while in all other cases the experimental collision frequencies are lower than the theoretical one. This discrepancy between the theoretical and experimental collision frequency might be caused by the fact that small droplets cannot be detected electrochemically and the droplets are not very stable and gradually grow larger with time in the presence of salts according to the Derjaguin-Landau-Verwey-Overbeek (DLVO) theory (Figure S4).[7,8] Besides, the hindered diffusion model[9] might also account for this discrepancy.

Table S4. Comparison between experimental and theoretical collision frequency. Note that experimental statistics is based on the data of Figure 1 in the main text.

Ions/Salts — Statistics	PF_6^- /TMAPF$_6$	Ac^- /TBAAc	ClO_4^- /TBAClO$_4$	PF_6^- /TEAPF$_6$	PF_6^- /TBAPF$_6$	THA^+ /THAPF$_6$
Amount of peaks	174	16	24	45	57	43
Experimental frequency/Hz	0.174	0.016	0.024	0.045	0.057	0.043
Theoretical frequency/Hz	0.11 (1 µm as the droplet radius in the calculation)					

5. Finite Element Simulations

The model of electron transfer coupled ion transfer at the droplet electrode was tested first in 1D and extended to 2D axis symmetry, utilizing COMSOL Multiphysics 5.2a. Effects of migration were assumed negligible, so two "Transport of Diluted Species" physics were utilized for diffusion of all the species, one in aqueous phase and the other in oil phase. The secondary current distribution was calculated with three "Electric Currents" physics, one for the electrode, one for the organic phase and one for the aqueous phase. The initial distribution of ions was calculated as described above. The potential ramp was done using a triangle function with 1 mV transition zone and two continuous derivatives. The general diffusion equation for a species i is:

$$\frac{\partial c_i}{\partial t} + \nabla \cdot \left(-D_i \nabla c_i \right) = 0 \tag{8}$$

where c is concentration, t is time and D is the diffusion coefficient for the species i. The species in the model are Rb and Rb^+ (present in oil phase phases) and C^+ and A^- present in both phases. The concentration boundary conditions were used at outer boundaries of the aqueous phase ($c_i =$ bulk concentration). The size of the aqueous phase was adjusted so that the microelectrode of the radius $r_{UME} = 5$ µm showed the limiting current within 1 % of what was expected from the theory (width and height 100 r_{UME}). The boundary conditions at the liquid-liquid interface were set as inward fluxes (N_i) according to the following reactions:

$$C^+(w) \underset{k_{IT,b}}{\overset{k_{IT,f}}{\rightleftarrows}} C^+(o) \qquad\qquad\qquad \text{(IT of } C^+ \text{ cation)} \qquad\qquad (9)$$

$$A^-(aq) \underset{k_{IT2,b}}{\overset{k_{IT2,f}}{\rightleftarrows}} A^-(o) \qquad\qquad\qquad \text{(IT of } A^- \text{ anion)} \qquad\qquad (10)$$

In the aqueous and oil phases the inward fluxes are

$$N_{w,\,C^+} = -k_{IT,f}\left[C^+(w)\right] + k_{IT,b}\left[C^+(o)\right] = -N_{o,\,C^+} \qquad\qquad (11)$$

$$N_{w,\,A^-} = -k_{IT2,f}\left[A^-(w)\right] + k_{IT2,b}\left[A^-(o)\right] = -N_{o,\,A^-} \qquad\qquad (12)$$

Here the unimolecular rate constants for ion transfer reactions (k_{IT} and k_{IT2}) are Butler-Volmer type rate constants depending on the Galvani potential difference $\Delta_o^w\phi$ with the expressions:

$$
\begin{aligned}
k_{IT,b} &= k_{IT}^0 \exp\left((\alpha-1)f\left(\Delta_o^w\phi - \Delta_o^w\phi_{C^+}^{0'}\right)\right) \\
k_{IT,f} &= k_{IT}^0 \exp\left(\alpha f\left(\Delta_o^w\phi - \Delta_o^w\phi_{C^+}^{0'}\right)\right) \\
k_{IT2,b} &= k_{IT2}^0 \exp\left((\alpha-1)f\left(\Delta_o^w\phi - \Delta_o^w\phi_{A^-}^{0'}\right)\right) \\
k_{IT2,f} &= k_{IT2}^0 \exp\left(\alpha f\left(\Delta_o^w\phi - \Delta_o^w\phi_{A^-}^{0'}\right)\right)
\end{aligned}
\qquad (13)
$$

where $f = F/RT$ and $\Delta_o^w\phi = \phi^w - \phi^o$ The α (charge transfer coefficient) for all the ion transfer reactions was set to 0.5. The unimolecular standard rate constants for ion transfer (k_{IT}^0 and k_{IT2}^0) were set to 0.02 cm s^{-1}. Typically, the ion transfer across the liquid-liquid interface is fast and reversible.[10] However, in the present case lower values are justified by the presence of the surface-active ionic liquid at the oil/water interface.[11] Here the transfer of the ionic liquid IL-PA is not considered. The transfer of the cation P_{66614}^+ was not observed within the potential window used in the experiments, indicating that it is very hydrophobic. The transfer of the anion NTf_2^- could have some effects, but due to the extreme hydrophobicity of the cation it is confined in the organic droplet.

Now, the oxidation of rubrene (Rb) was considered to take place at the oil-electrode interface:

$$Rb(o) \underset{k_{o,red}}{\overset{k_{o,ox}}{\rightleftarrows}} Rb^+(o) + e^- \qquad\qquad\qquad\qquad (14)$$

Now, the inward fluxes at the oil side are

$$N_{o,\,Rb} = -N_{o,\,Rb^+} = -k_{o,ox}\big[Rb(o)\big] + k_{o,red}\big[Rb^+(o)\big] \qquad (15)$$

where the rate constants for oxidation and reduction are expressed as

$$
\begin{aligned}
k_{o,red} &= k_o^0 \exp\!\Big((\alpha-1)f\big(E - \big[E^{0'}_{Rb^+/Rb}\big]_o\big)\Big) \\
k_{o,ox} &= k_o^0 \exp\!\Big(\alpha f\big(E - \big[E^{0'}_{Rb^+/Rb}\big]_o\big)\Big)
\end{aligned}
\qquad (16)
$$

Here the potential of the electrode is defined as $E = \phi^E - \phi^o$, where ϕ^E is the Galvani potential of the electrode. k_o^0 was set as 0.02 cm s^{-1} and all values of α were set to 0.5. Again, this low value of k_o^0 is justified by the by the presence of the surface-active ionic liquid at the droplet surface.[11]

The governing equations of the "Electric Currents" physics are:

$$\mathbf{J} = \sigma^\alpha \mathbf{E} = -\sigma^\alpha \nabla \phi^\alpha \qquad (17)$$

where $\mathbf{J}$ and $\mathbf{E}$ are current density and electric field (both are vector variables), σ^α is conductivity and ϕ^α is the Galvani potential of the phase α. Measured conductivities of the organic phase (155 μS/cm measured with 400 mM of the ionic liquid in toluene) and aqueous phase (376 μS/cm measured with 5 mM TBAClO$_4$) were used for all simulations. Three physics, one for each phase, were used. This equation is Ohm's law for the current and the potential. The potential at the outer boundary of the metal 5 μm away from the electrode surface was given values of the potential ramp, and the potential at the outer boundary of the aqueous phase was grounded. The boundary conditions were set utilizing the inward current density:

$$J_E = FN_{w,\,Rb} = F\big(-k_{o,ox}\big[Rb(o)\big] + k_{o,red}\big[Rb^+(o)\big]\big) = -J_o \text{ (at electrode-droplet interface)} \quad (18)$$

$$J_o = F\big(N_{o,\,C^+} - N_{o,\,A^-}\big) = F\big(k_{IT,f}\big[C^+(w)\big] - k_{IT,b}\big[C^+(o)\big] - k_{IT2,f}\big[A^-(w)\big] + k_{IT2,b}\big[A^-(o)\big]\big) = -J_w$$

$$\text{(at the liquid-liquid interface)} \qquad (19)$$

When solving the system, the Galvani potential of the droplet ϕ^O is floating so that J_E, J_w and J_o have the same magnitude.

The droplet on the electrode was estimated as a polar cap of a sphere with the same volume of the spherical droplet in the solution. Droplet with a radius r_d on the electrode surface was estimated as a polar cap with the height of $h = f \times r_d$, where f gets values between 0 and 2. For example, a droplet with a radius of 2 µm, will form a polar cap of the height of 1.4 r_d = 2.8 µm, with its radius on the electrode ($r_{d,surface}$, Figure S6) of 2.29 µm, and the radius of the interface with the electrode (r_e, Figure S6) of 2.24 µm. The equations relating the polar cap dimensions to the original droplet (volume of the droplet in bulk V_d, volume of the polar cap V_{cap}, r_e, and $r_{d,surface}$) can all be calculated when r_d and $h = f \times r_d$ are defined. The simulation parameters are tabulated in Table S5.

$$V_d = \frac{4}{3}\pi r_d^{\ 3} \tag{20}$$

$$V_{cap} = \frac{\pi h}{6}\left(3r_e^{\ 2} + h^2\right) = V_d \tag{21}$$

$$r_e = \sqrt{\frac{1}{3}\left(\frac{6V_d}{\pi h} - h^2\right)} \tag{22}$$

$$r_{d,\,surface} = \frac{r_e^{\ 2} + h^2}{2h} \tag{23}$$
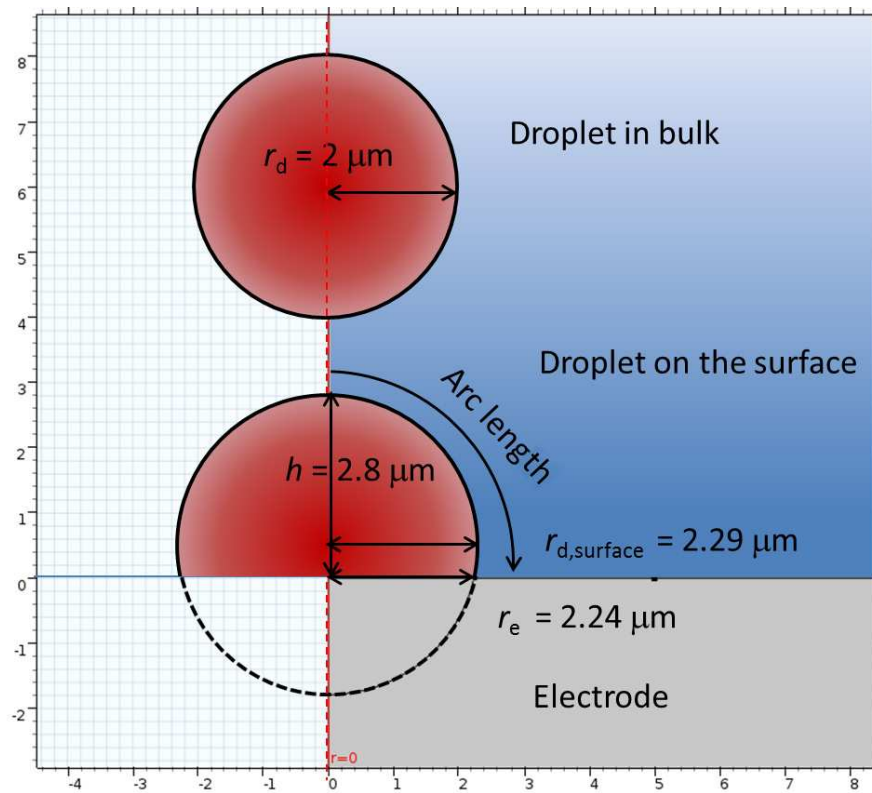
Figure S6. Estimated droplet geometry on the electrode surface in the COMSOL model.

Table S5. Parameters used in the COMSOL model.

Parameter	Value	Justification
D_{aq}	11×10^{-6} cm^2 s^{-1}	Chosen from values calculated from limiting conductivities of salts.
D_o	17.7×10^{-6} cm^2 s^{-1}	Calculated with Walden's rule from viscosities of pure solvents (0.890 mPas for water, 0.553 mPas for toluene)
D_{Rb}, D_{Rb^+}	2.21×10^{-6} cm^2 s^{-1}	From ref.[12]
Scan rate	40 V s^{-1}	
k_o^0	0.02 cm s^{-1}	Rate constant slightly slowed by the surfactant layer
k_{IT}^0, k_{IT2}^0	0.02 cm s^{-1}	Rate constant slightly slowed by the surfactant layer
α	0.5	Assumption
$\Delta_o^w \phi_{A^-}^{0'}$, $\Delta_o^w \phi_{C^+}^{0'}$	Values from Table S1	
$\left[E_{Rb^+/Rb}^{0'} \right]_o - E_{Ref}$	0.45 V	Fitted from experimental data
Droplet radius r_d	2 µm	Fitted from experimental data
Cap Height	$h = 1.4 \, r_d$	Fitted from experimental data
Concentrations	5 mM	Electrolyte in aqueous phase, Rb in organic phase.

The full 2D axis symmetry model took *ca*. 17 h to solve with Intel Core quad-core i-7-4870HQ CPU @2.50 GHz, with 16 GB of RAM (MacBook Pro running Windows 7 as the operating system). The 2D axis symmetrical model was tested by simulating oxidation of rubrene on the 5 µm radius microelectrode, at scan rates of 10 mV/s and 40 V/s (*viz*. 20 Hz in Figure 1 in the main text). The simulations results are shown in Figure S7. The simulated steady state current (red line in Figure S7) showed 1 % deviation from the value expected from theory, while the

transient limiting current (black line) shown in Figure S7 was *ca*. 3 % higher than expected from the theory, with the same mesh density. Hence, numerical errors in the simulations of droplets are expected to be of the similar range.
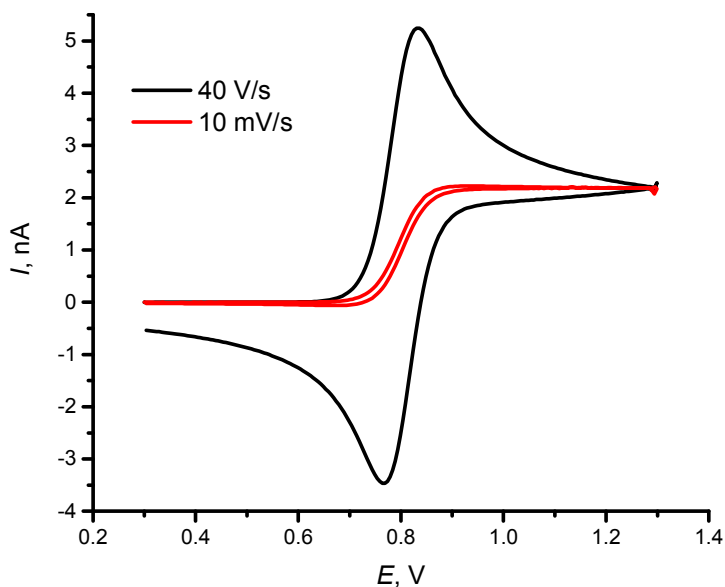

Figure S7. Oxidation of 5 mM of rubrene on the 5 μm radius microelectrode at scan rates of 10 mV/s and 40 V/s.

The best match with the experimental data is shown in Figure 2D in the main text, with parameters described in Table S5. The model gives also additional information, like current distribution, shown in Figure S8. The current distribution at the liquid-liquid interface (arc length of 0 is the cap of the droplet while 4 μm corresponds to the droplet boundary contacting with the electrode surface) shows that ion transfer takes place rather uniformly over the whole interface, with some preference towards the reaction closer to the electrode. On the other hand, the electrode reaction shows a uniform current distribution, with a sharp increase in the activity close to the three-phase boundary, which is partially in agreement with previous speculation.[12]

Figure S9 shows the concentrations of Rb^+, anion in the aqueous phase and anion in the organic droplet at the potential of 1.1 V, as well as the stream lines for the current, and Figure S10 shows the Galvani potentials of the phases. These figures show that diffusion of Rb^+ is the limiting factor, and the high diffusion coefficient of anions in toluene phase results in very small difference in concentration distribution within the droplet. No significant Ohmic drop is observed at these current densities, as the Galvani potential is practically constant.
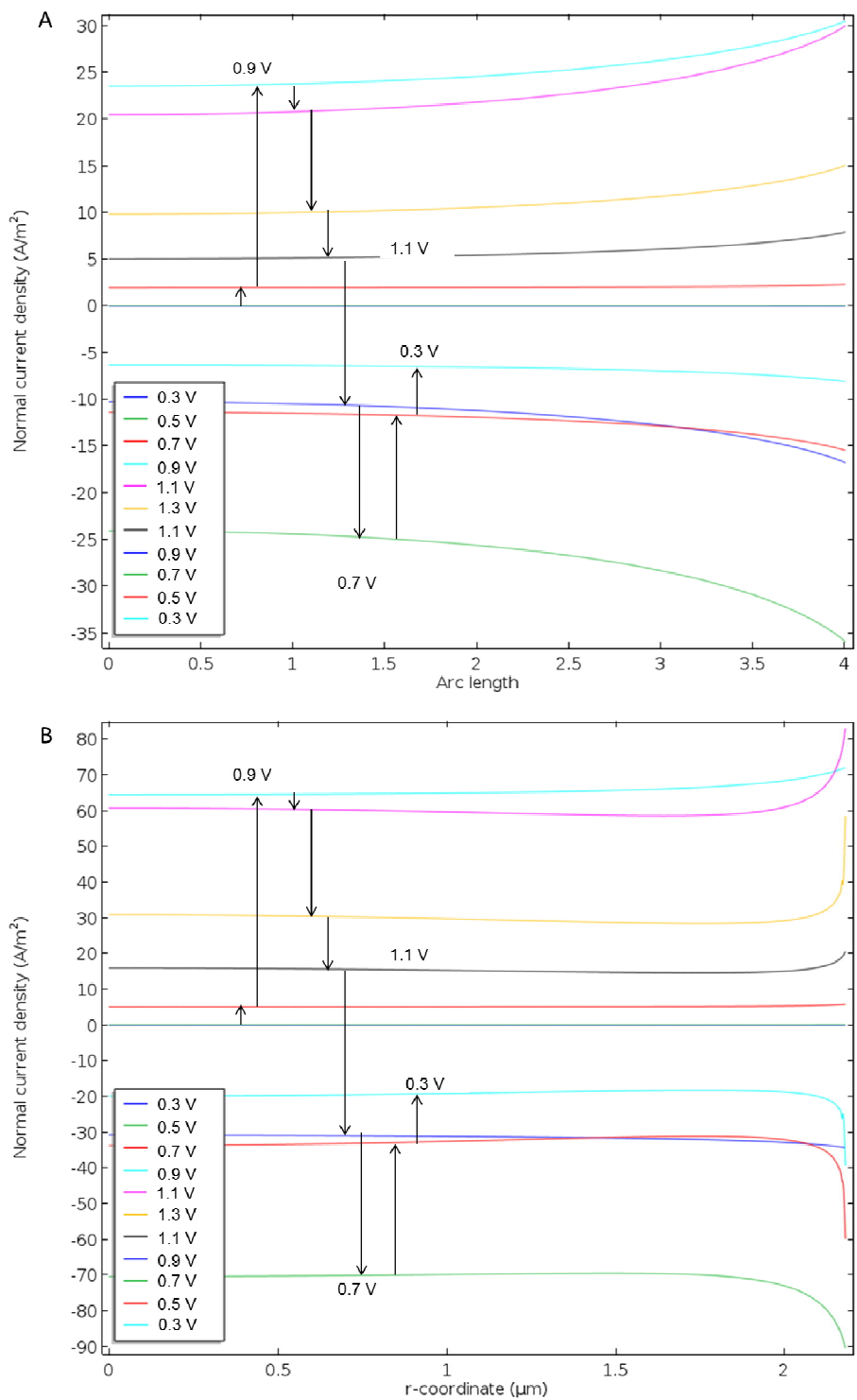
Figure S8. (**A**) The current density at the liquid-liquid interface (**B**) and at the electrode-droplet interface at different potentials.
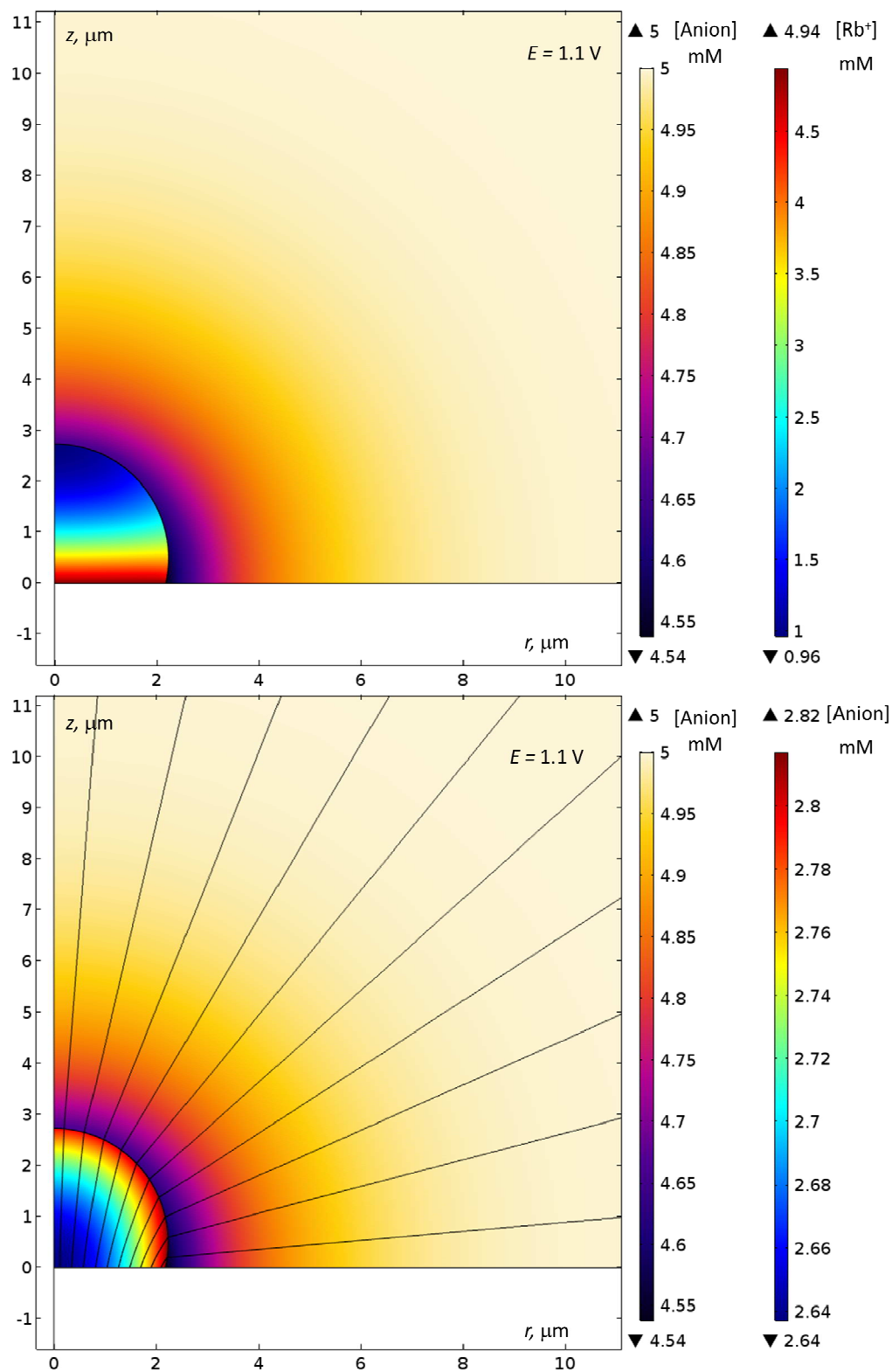
Figure S9. A snapshot of the simulation at the $E = 1.1$ V, showing the concentrations of the oxidized rubrene, and anions in the aqueous phase and organic phase.
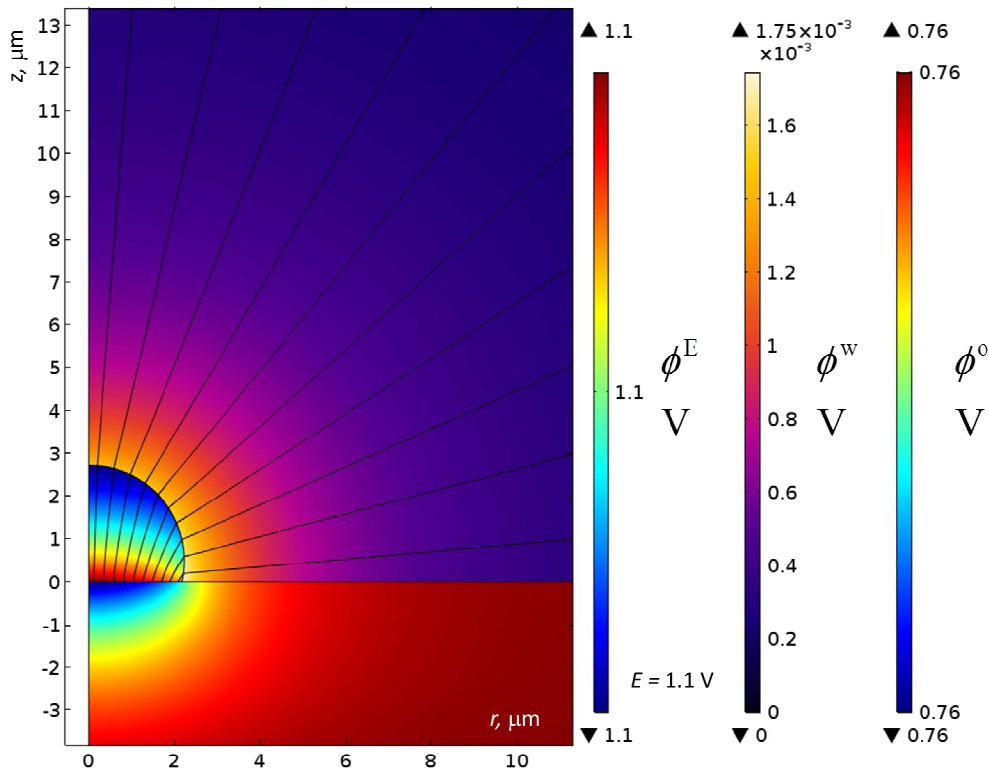
Figure S10. A snapshot of the simulation at the $E = 1.1$ V, showing the small variations in the Galvani potentials of the phases.

The effect of the droplet size was also investigated, with parameters described in Table S5, and the results are shown in Figure 4 in the main text. As the droplet size gets smaller, the voltammetry starts to resemble the thin-layer cell,[13,14] as diffusion of the redox mediator is confined to smaller space. The peak current is directly proportional to the surface area of the electrode contacting with the droplet, and the radius of this base of the spherical cap is directly proportional to the droplet radius:

$$r_e = \sqrt{\frac{1}{3h}\left(8r_d^3 - h^3\right)} = \sqrt{\frac{1}{3f}\left((8 - f^2)r_d^2\right)} = r_d\sqrt{\frac{(8 - f^2)}{3f}} \tag{24}$$

$$A_{\text{UME/o}} = \pi r_e^2 = \frac{(8 - f^2)}{3f}\pi r_d^2 \tag{25}$$

This is illustrated in Figure S11.
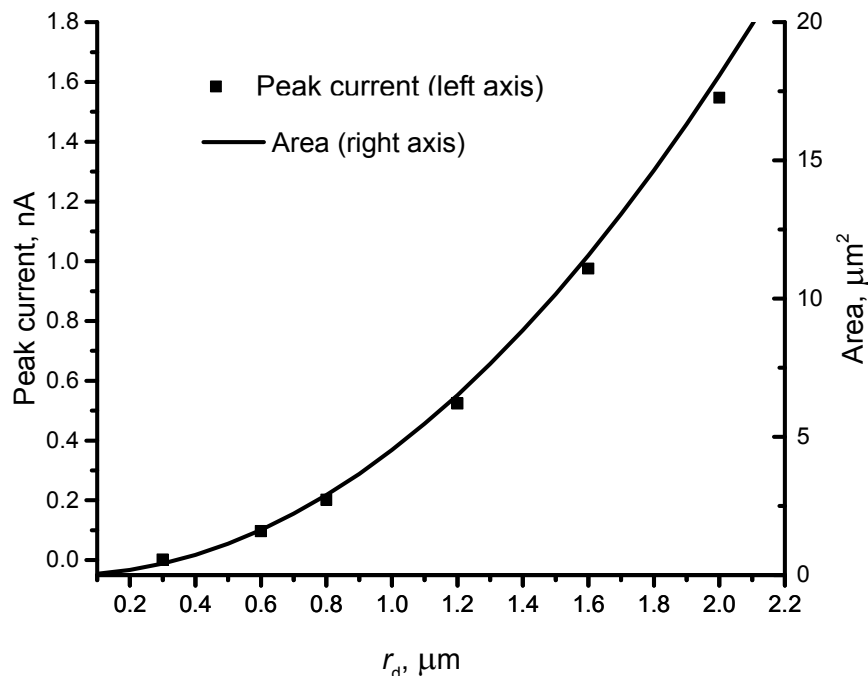
Figure S11. Dependence of the simulated oxidation peak current on the droplet radius, and dependence of the droplet/electrode area on the droplet radius (Eq. 25), $h = 1.4\,r_d$.

Additionally, the effect of the kinetic parameters was investigated in a parametric sweep resulting in 16 simulations. The effect of changing the standard rate constants is illustrated in Figures S12 (variation of the ion transfer rate while keeping the electron transfer rate constant) and S13 (variation of the electron transfer rate while keeping the ion transfer rate constant). Figures S12 and S13 show that electron transfer reaction has the biggest impact: decreasing standard rate constants results in decreasing peak currents and wider peak separation. Decreasing standard rate constants of the ion transfer reaction does not significantly affect the peak current, but increases the peak separation, especially at low values of $k_{IT}^0 < 0.01$ cm s^{-1}. A qualitative agreement with the experimental FSCV is obtained with both k_{IT}^0 and k_{ET}^0 of *ca.* 0.01 cm s^{-1}.
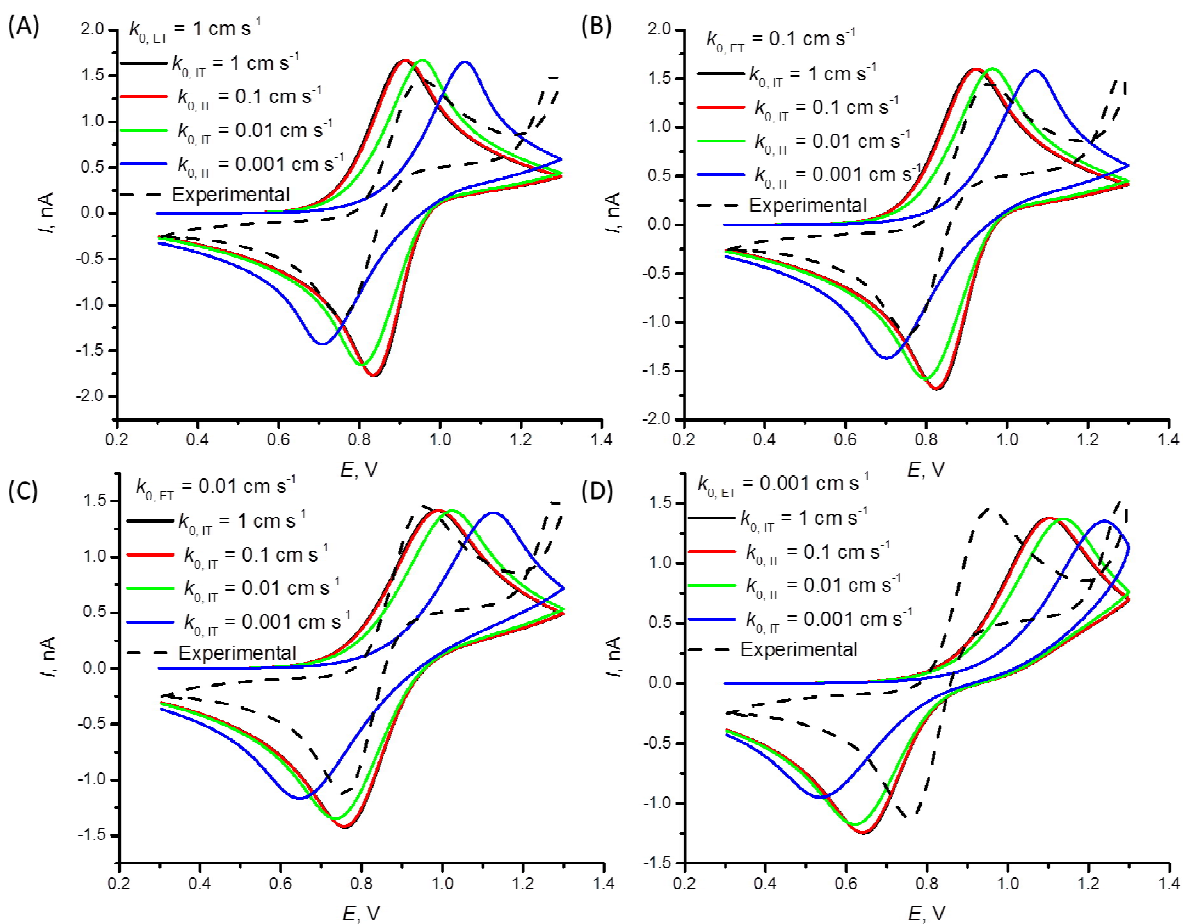
Figure S12. The effect of changing the standard ion transfer rate constant with constant electron transfer rate in which the experimental CV (black dashed line) is included for comparison: (A) $k_{0, ET}$ = 1 cm s^{-1}, $k_{0, IT}$ varies from 0.001 to 1 cm s^{-1} (B) $k_{0, ET}$ = 0.1 cm s^{-1}, $k_{0, IT}$ varies from 0.001 to 1 cm s^{-1} (C) $k_{0, ET}$ = 0.0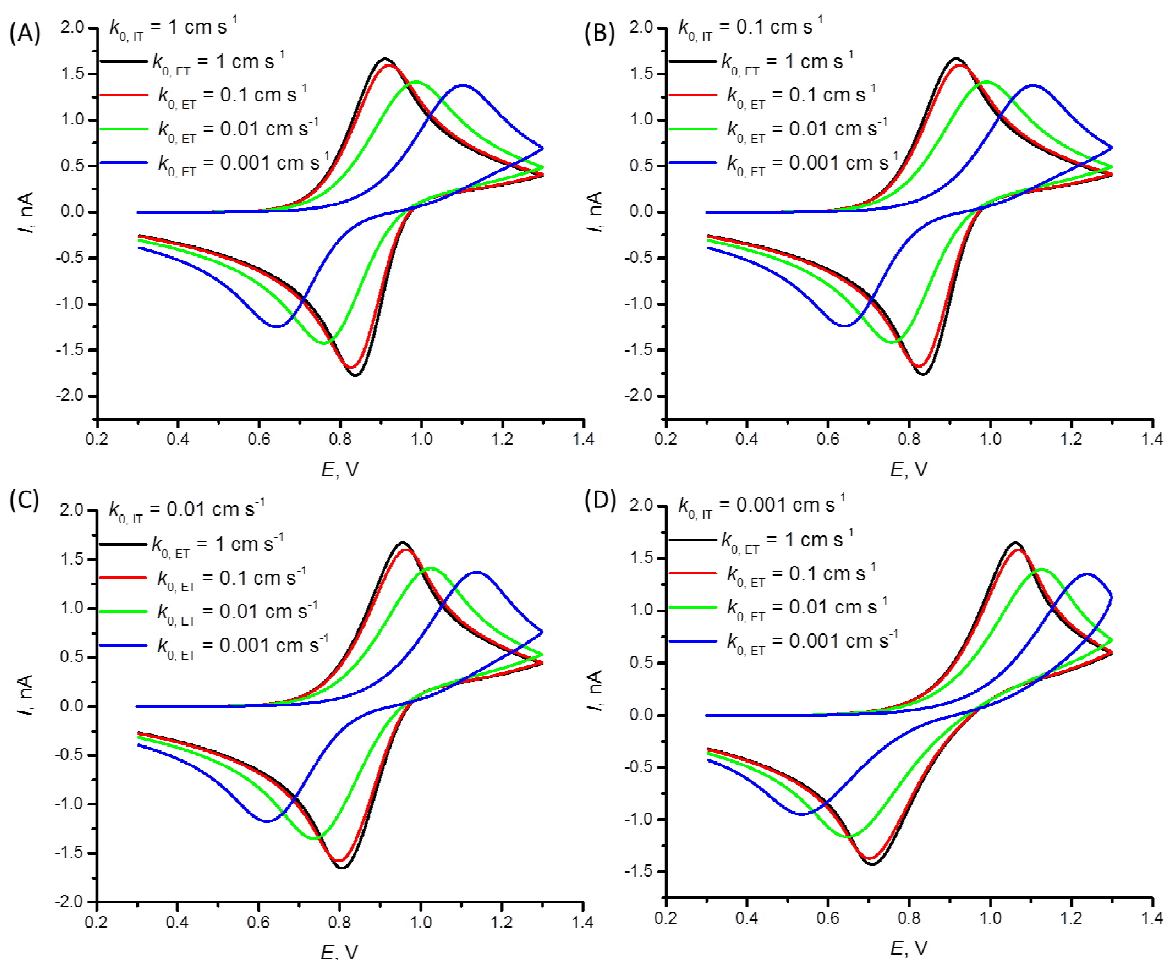1 cm s^{-1}, $k_{0, IT}$ varies from 0.001 to 1 cm s^{-1} (D) $k_{0, ET}$ = 0.001 cm s^{-1}, $k_{0, IT}$ varies from 0.001 to 1 cm s^{-1}.

Figure S13. The effect of changing the standard electron transfer rate constant with constant ion transfer rate: (A) $k_{0, IT} = 1$ cm s^{-1}, $k_{0, ET}$ varies from 0.001 to 1 cm s^{-1} (B) $k_{0, IT} = 0.1$ cm s^{-1}, $k_{0, ET}$ varies from 0.001 to 1 cm s^{-1} (C) $k_{0, IT} = 0.01$ cm s^{-1}, $k_{0, ET}$ varies from 0.001 to 1 cm s^{-1} (D) $k_{0, IT} = 0.001$ cm s^{-1}, $k_{0, ET}$ varies from 0.001 to 1 cm s^{-1}.

Figures S12 and S13 show that the electron transfer reaction has more significant influence on the overall reaction rate, but this is because the area available for the reaction is smaller than the area available for the ion transfer. Hence, it seems that the standard rate constant for the electron transfer is ca. 0.01 cm s^{-1} while the rate constant for the ion transfer can be between 10 to 0.01

cm s^{-1}. Experiments with smaller ion transfer area would be required to conclude something more definitive about the ion transfer rate. Also, in this case the inward surface of the droplet is covered by the cation of the ionic liquid, and this will affect both electron and ion transfer rates.

   The charge transfer coefficient of the ion transfer reaction did not have any noticeable effect when varied among the values from 0.1 to 0.9, while increasing α_{ET} increased the oxidation peak current and reduced the reduction peak current as shown in Figure S14. The deviation of α_{ET} from 0.5 could be justified due to the Frumkin effect on the electric double layer of the surfactant covered electrode in a solvent of low relative permittivity.[15] However, this approach would require detailed analysis of the electric double layer within the droplet. As the effect of the α_{ET} is not very significant, this detailed analysis is left outside the scope of this work.
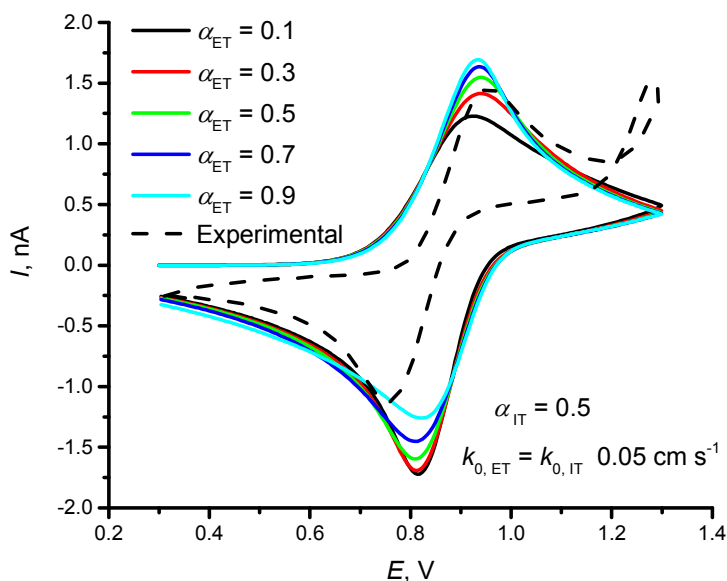

Figure S14. The effect of charge transfer coefficient of the electron transfer reaction on the simulated FSCV.

It should be noted that the system could be also simulated with two "Nernst-Planck" physics to account for mass transport and current flow in both the aqueous and organic phases, respectively. However, the tertiary current distribution is more computationally intensive, and ion paring should be considered to obtain the experimentally measured conductivity. The simulation was tested for the same parameters as listed in Table S5, and the comparison is shown in Figure S15. It is seen that the differences are small (black *vs*. red colored curves), so the usage of the simplified model is justified.
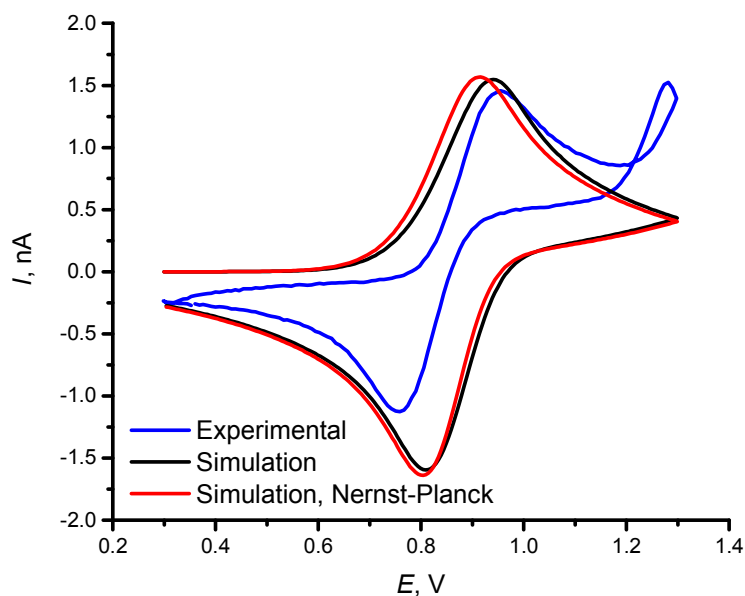

Figure S15. Comparison of the experimental voltammogram of 5 mM TBAAc at 40 V s^{-1} (blue line) with the simulated voltammograms, considering secondary current distribution with diffusion (black line), or tertiary current distribution (red line with the Nernst-Planck model).

6. TBAAc Concentration Effect

Next we investigated the evolution of the FSCV of the single emulsion collision *via* the electron transfer coupled ion transfer process as a function of TBAAc concentration in the aqueous phase. Note that rubrene is in 5 mM in toluene and the initial TBAAc concentration varies from 0.1 mM to 200 mM in the aqueous, as shown in Figure S16. The overall potential E applied at the UME for the case of anion transfer across w/o interface coupled with rubrene redox reaction at the UME/o interface can be expressed as follows,[12,16,17]

$$E - E_{\text{ref}}^{\circ} = \Delta_{\text{o}}^{\text{UME}}\phi - \Delta_{\text{o}}^{\text{w}}\phi \tag{26}$$

where the potential difference of the UME (E) *vs.* the reference electrode potential in the aqueous phase (E_{ref}°), $E - E_{\text{ref}}^{\circ}$, is split into two components: $\Delta_{\text{o}}^{\text{UME}}\phi$, which represents the redox potential of rubrene; and $\Delta_{\text{o}}^{\text{w}}\phi$ ($\Delta_{\text{o}}^{\text{w}}\phi = \phi^{\text{w}} - \phi^{\text{o}}$), the Galvani potential difference across the liquid/liquid interface that has been defined before. Eq. 26 can be rewritten as in Eq. 27.[18]

$$E - E_{\text{ref}}^{\circ} = \left[E_{\text{Rb}^+/\text{Rb}}^{\ominus'} \right]_{\text{SHE}}^{\text{o}} + \frac{RT}{F}\ln\left(\frac{c_{\text{Rb}^+}}{c_{\text{Rb}}} \right) - \left(\Delta_{\text{o}}^{\text{w}}\phi_i^{\ominus'} + \frac{RT}{z_i F}\ln\left(\frac{c_i^{\text{o}}}{c_i^{\text{w}}} \right) \right) \tag{27}$$

where $\left[E_{\text{Rb}^+/\text{Rb}}^{\ominus'} \right]_{\text{SHE}}^{\text{o}}$ is the formal redox potential of the Rb$^+$/Rb redox couple in the organic phase *vs.* aqueous SHE electrode, c_{Rb^+} and c_{Rb} are the concentrations of Rb$^+$ and Rb on the UME surface under equilibrium, $\Delta_{\text{o}}^{\text{w}}\phi_i^{\ominus'}$ is the formal ion transfer potential of species i with a charge number z_i including the sign ("–" for anion) across the w/o interface that is a constant, c_i^{w} and c_i^{o} are the concentrations of the species i at the aqueous and organic sides of the liquid/liquid interface under equilibrium, respectively, R, T, and F have been defined previously. So potential

E applied at the UME affects both concentration ratios of c_{Rb^+}/c_{Rb} and c_i^o/c_i^w. At the half-wave potential $E_{1/2}$ the concentration ratio of a limiting redox or ionic couple will be 1, if both species have the same diffusion coefficients. At small concentrations of TBAAc in the aqueous phase c_i^o/c_i^w will be 1 at the half-wave potential $E_{1/2}$, and at higher concentrations $c_{Rb^+}/c_{Rb}=1$ at $E_{1/2}$. Figures S16A and B show that E applied at the UME which represents as the $E_{1/2}$ of CV increases with the increase in aqueous Ac$^-$ concentration. However, $E_{1/2}$ is expected to increase firstly with the increase in TBAAc concentration and then decrease with even higher TBAAc concentration (see Figure S17), as the reaction changes from anion transfer limited case into the electron transfer limited case while increasing the TBAAc concentration in the aqueous phase.[16] Accordingly $E_{1/2}$ is influenced by the ratio of c_i^o/c_i^w at the o/w interface at low concentrations of TBAAc. However, the experimentally determined $E_{1/2}$ continues to increase with increasing Ac$^-$ concentration in aqueous, as shown in Figures S16B and C. This apparently abnormal behavior indicates that electron transfer never becomes the limiting step. This is also supported by the decreasing currents observed at higher concentrations of Ac$^-$ (Figure S16A). This could be due to precipitation of Ac$^-$ in the organic phase, either with the supporting electrolyte cation or Rb$^+$, ion pairing in the organic phase, or also the instability of the QRE.
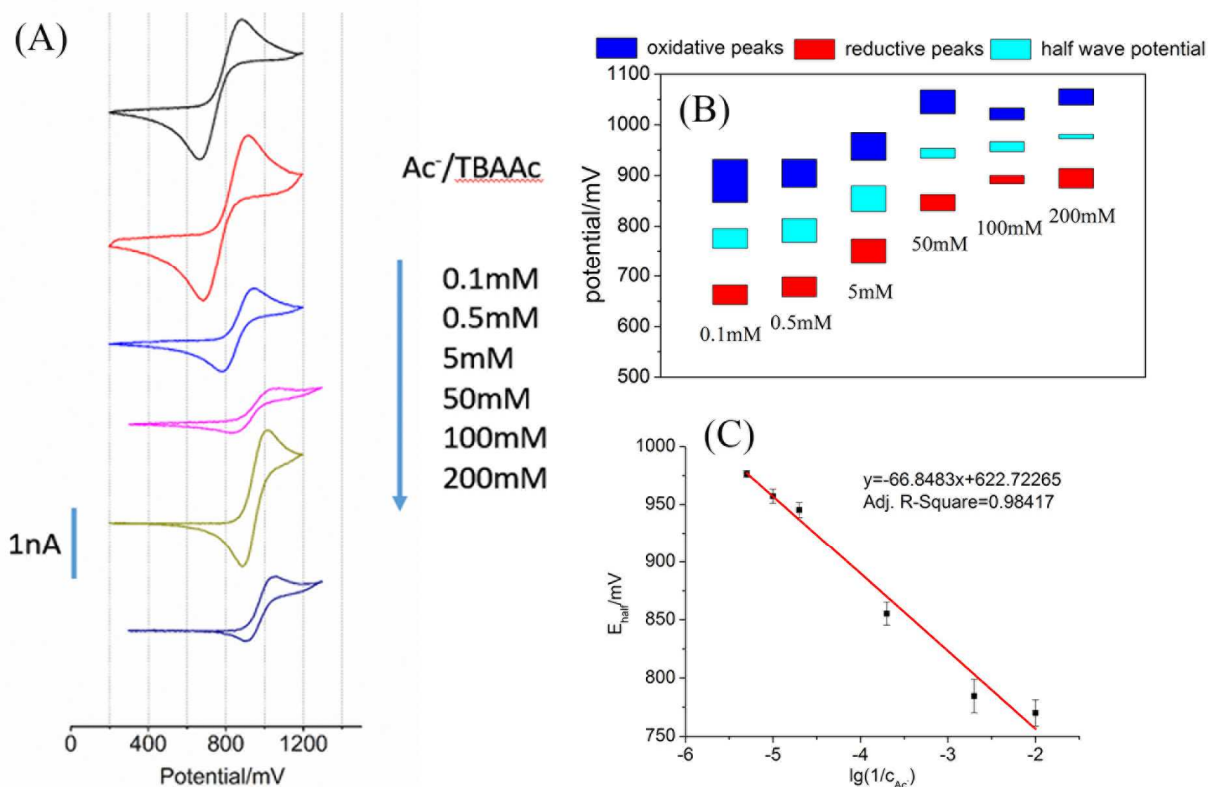
Figure S16. (A) The recovered CVs of electron transfer coupled with Ac⁻ ion transfer at w/o interface as a function of aqueous Ac⁻ concentration corresponding to single emulsion droplet colliding on the C UME recorded by FSCV. The concentrations of TBAAc in aqueous phase from top to bottom were 0.1 mM, 0.5 mM, 5 mM, 50 mM, 100 mM, and 200 mM, respectively. (B) The range bar chart of peak and half-wave potentials of obtained collision signals from Figure S16A. Approximate 10 independent collision experiments for each Ac⁻ concentration were analyzed for making this chart. (C) The dependence of $E_{1/2}$ (*i.e.* E_{half}) on the logarithm of reciprocal of aqueous Ac⁻ concentration.

The effect of the concentration of TBAAc in aqueous on the shape of the voltammogram was simulated, with parameters described in Table S5, for r_d of 0.6 µm and 2 µm, with $h = 1.4\ r_d$. The results are shown in Figure S17.
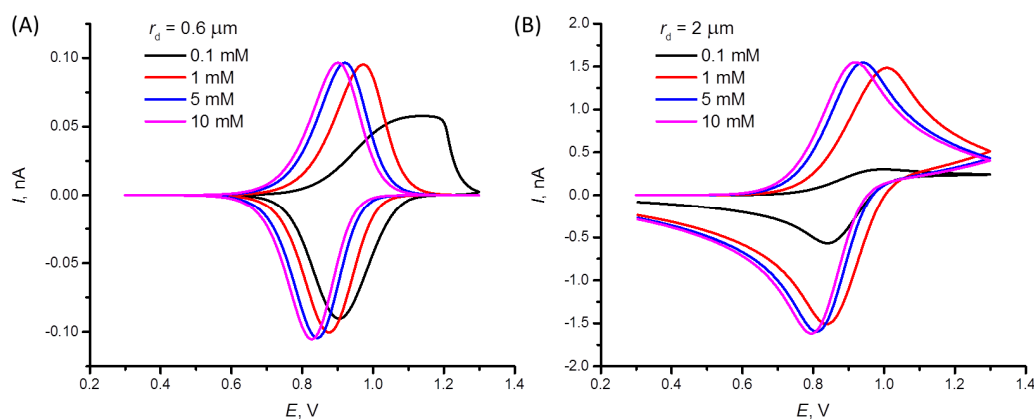
Figure S17. Effect of the TBAAc concentration in the aqueous phase on the FSCV, $h = 1.4\ r_d$. **(A)** $r_d = 0.6$ μm and **(B)** $r_d = 2$ μm. All other parameters are the same as in Table S5.

When the droplet is small, the diffusion length within the droplet decreases, resulting in thin-layer cell type behavior when the mass transfer of rubrene limits the coupled ET-IT reaction. However, when mass transfer of the anion from the aqueous phase to the droplet is the limiting process, on the forward scan hemispherical diffusion is observed, resulting in a sigmoidal wave (black curve in Figure S17A). Now the decay at high potentials is due to the depletion of rubrene within the droplet, so the system switches from anion transfer controlled reaction into the reaction limited by mass transfer of rubrene on the electrode surface. On the reverse scan, thin-layer type behavior is observed because the transferred anion has been concentrated in the aqueous side (black curve in Figure S17A). However, if the droplet size is increased, the diffusion lengths also increase and voltammetry starts to resemble systems limited by linear diffusion (Figure S17B). If the concentration of the transferring anion in the aqueous phase is low enough to limit the rate of the overall process, voltammogram shows a sigmoidal shape due to the hemispherical diffusion of the anion in the aqueous phase (black curve in Figure S17B),

but now there is no decay in the current as there is larger amount of rubrene available in the droplet.

To investigate further the voltammetry with varying amounts of TBAAc, the system was simulated in 1D and similar behavior as earlier observed by Dassie *et al.*[16] was reproduced. Figure S18 shows the half-wave potential obtained from 1D simulations for the case where all the species have, the same diffusion coefficients, or when the diffusion coefficients in Table S5 were used. Comparison between the experimental data and the simulated data with ionic association and precipitation is also included.
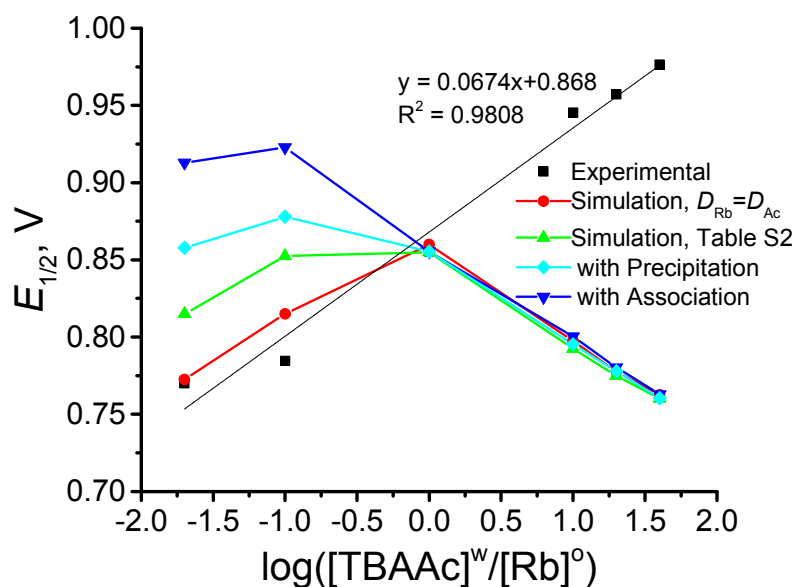

Figure S18. Effect of the concentration of TBAAc in the aqueous phase on the half-wave potential observed in the CV, with 5 mM of Rb in the organic phase. Simulations were done with the 1D model, considering equal diffusion coefficients of all the species, or diffusion coefficients as in Table S5. Association of Rb^+ with Ac^- was considered with $K_{ass} = 1 \times 10^5$ L mol^{-1} and $k_{-1} = 1 \times 10^9$ s^{-1} and precipitation of RbAc was considered with $K_{sp} = 1 \times 10^{-6}$ mol L^{-1} and $k_d = 10$ s^{-1}. The half-wave potential has been adjusted so that the value at equal concentrations of TBAAc and Rb is the same for all the simulations.

To investigate the origin of the deviation from the theoretical behavior, simulations were done considering association with rubrene cation ($Rb^+ + A^- \underset{k_{-1}}{\overset{k_1}{\rightleftharpoons}} RbA$, $K_{ass} = k_1 / k_{-1}$) , but the experimentally observed behavior could not be reproduced exactly. Association only shifted the observed wave towards more negative potentials, and this shift became larger with increasing equilibrium constant for association (Figure S19). Additionally, the peak current for the forward wave increased compared to the case without association, while the peak current for the backward wave decreased with increasing association constant. Hence, association could also explain the discrepancy between the experimental and simulated FSCV in Figure 2D in the main text. Precipitation of rubrene cation with acetate (Herein A^- represents anions inside the toluene droplet like acetate) was considered as well ($Rb^+ + A^- \underset{k_d}{\overset{k_p}{\rightleftharpoons}} RbA(s)$, $K_{sp} = k_d / k_p$ where K_{sp} is the solubility product, k_d is the dissolution rate and k_p is the precipitation rate). In this case, the activity of the precipitate is unity when there is any precipitate present, and 0 when everything has dissolved. This was implemented by setting the activity as $a_{RbA(s)} = c_0 \left(1 - \exp\left(-1000 c_{RbA(s)} / c_0 \right) \right)$, where c_0 is the standard concentration of 1 M. This function can be considered as a step function, but it is smoother, making it easier for the numerical solver to handle. Whereas this is not a very accurate way to describe precipitation, it serves as an indication of how the precipitation would affect the FSCV. The effect of precipitation of rubrene cation with acetate (simulated CVs not shown) is similar to that of association between rubrene cation and acetate. The simulated results have been added in Figure S19. It should be stressed that the exact mechanism behind the anomaly at higher aqueous analyte concentration in Figures S16 and S18 needs to be further investigated in our future studies.
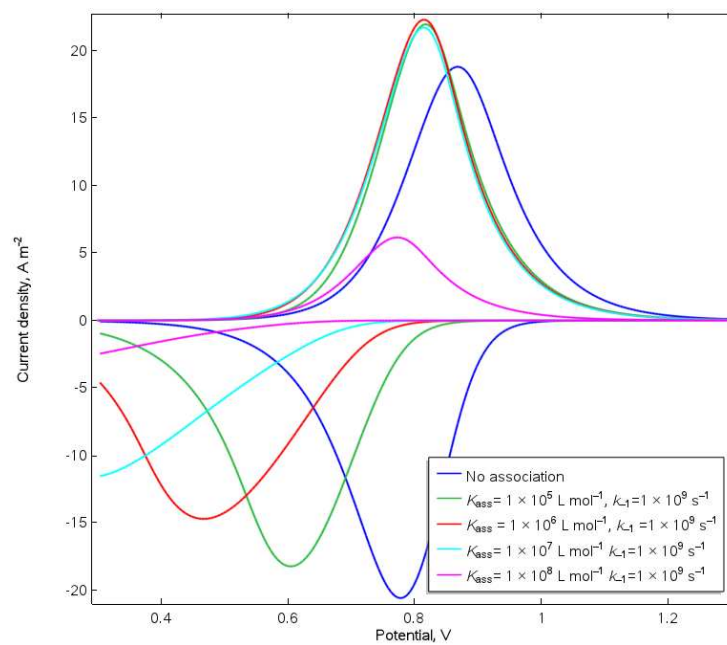
Figure S19. Effect of association equilibrium constant on the voltammetry, with 5 mM TBAAc in the aqueous phase and 1D model.

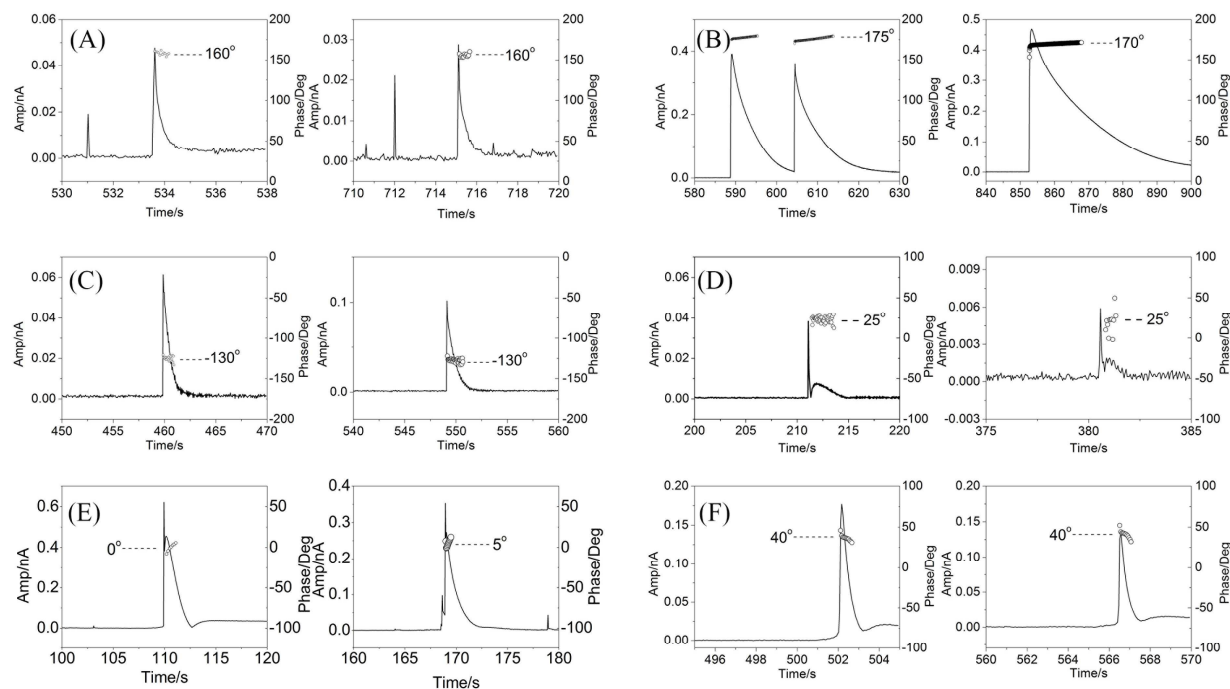# 7. Phase Angle Analysis and Collision Mechanisms

Figure S20. The second order harmonic background subtracted magnitude (——) and phase angle (○) components corresponding to the emulsion droplets collision experiments shown in Figure 1 in the main text with the addition of (A) 5 mM $TMAPF_6$, (B) 5 mM TBAAc, (C) 5 mM $TBAClO_4$ dissolved in aqueous phase, and (D) 5 mM $THAPF_6$, (E) 5 mM $TBAPF_6$, (F) 5 mM $TEAPF_6$ dissolved in toluene phase, respectively.
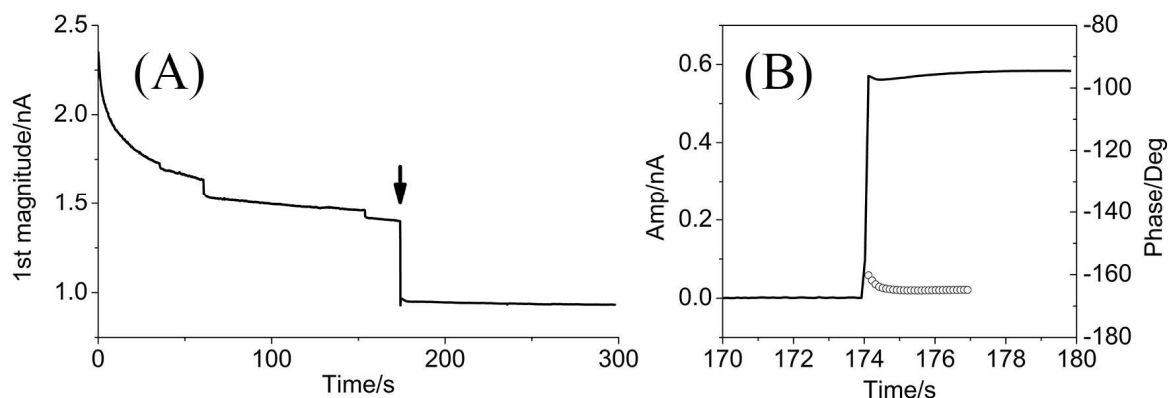
Figure S21. (A) The first order magnitude component of current response obtained by FTSV at a Pt UME with pure toluene emulsion droplets (400 mM IL–PA) without any redox probe or salt dissolved in either toluene or aqueous phase. The parameter setting was the same as Figure 1 in the main text. The black arrow marked the fusion event of an emulsion droplet, which was analyzed in (B). (B) The background subtracted magnitude (absolute value) and phase angle component of marked collision event presented in (A).

8. References

(1) Kakiuchi, T. In *Liquid-Liquid Interfaces Theory and Methods*; CRC Press, 1996, pp 1-18.
(2) Kasuno, M.; Matsuyama, Y.; Iijima, M. *ChemElectroChem* **2016**, *3*, 694-697.
(3) Zhou, M.; Gan, S.; Zhong, L.; Su, B.; Niu, L. *Anal. Chem.* **2010**, *82*, 7857-7860.
(4) Stockmann, T. J.; Ding, Z. *J. Electroanal. Chem.* **2010**, *649*, 23-31.
(5) Kim, B.-K.; Boika, A.; Kim, J.; Dick, J. E.; Bard, A. J. *J. Am. Chem. Soc.* **2014**, *136*, 4849-4852.
(6) Kestin, J.; Sokolov, M.; Wakeham, W. A. *J. Phys. Chem. Ref. Data* **1978**, *7*, 941-948.
(7) Levine, S. *Proc. R. Soc. Lond. A* **1939**, *170*, 145-164.
(8) Levine, S. *Proc. R. Soc. Lond. A* **1939**, *170*, 165-182.
(9) Eloul, S.; Compton, R. G. *J. Phys. Chem. Lett.* **2016**, *7*, 4317-4321.
(10) Samec, Z. *Electrochim. Acta* **2012**, *84*, 21-28.
(11) Strutwolf, J.; Manzanares, J. A.; Williams, D. E. *Electrochem. Commun.* **1999**, *1*, 139-144.
(12) Deng, H.; Dick, J. E.; Kummer, S.; Kragl, U.; Strauss, S. H.; Bard, A. J. *Anal. Chem.* **2016**, *88*, 7754-7761.
(13) Hubbard, A. T. *J. Electroanal. Chem.* **1969**, *22*, 165-174.

(14) Tom, G. M.; Hubbard, A. T. *Anal. Chem.* **1971**, *43*, 671-674.

(15) Bard, A. J.; Faulkner, L. R. *Electrochemical Methods*, 2nd ed.; John Wiley & Sons: New York, 2001.

(16) Zanotto, F. M.; Fernández, R. A.; Dassie, S. A. *J. Electroanal. Chem.* **2017**, *784*, 25-32.

(17) Zhao, W.; Yin, X.; Gao, Y.; Xie, X.; Liu, S.; Li, B.; Ji, T.; Zhu, Z.; Li, M.; Shao, Y. *J. Electroanal. Chem.* **2012**, *677–680*, 113-119.

(18) Samec, Z. *Pure Appl. Chem.* **2004**, *76*, 2147-2180.